EES Batteries

rsc.li/EESBatteries

ROYAL SOCIETY
OF **CHEMISTRY**
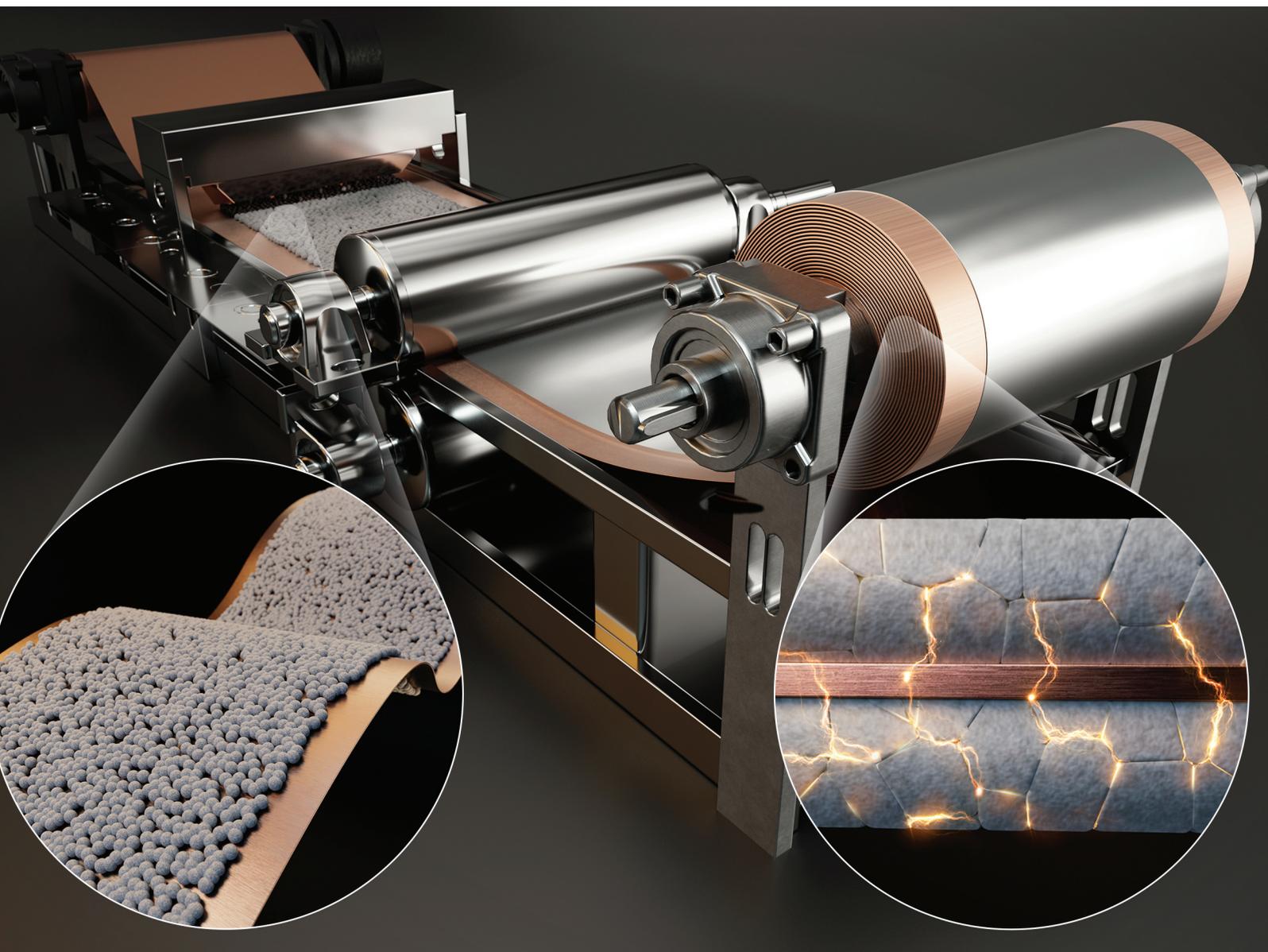
PAPER
Yong Min Lee *et al.*
Calendering-induced interfacial reconfiguration enables
electrochemical activation in lithium metal powder
electrodes for high-energy-density batteries

PAPER

Calendering-induced interfacial reconfiguration enables electrochemical activation in lithium metal powder electrodes for high-energy-density batteries

Dongyoon Kang, [ID] †[a] Sun Hyu Kim, [ID] †[b] Jaejin Lim, [ID] †[a] Hayeon Kim, [ID] [b]
Cyril Bubu Dzakpasu, [ID] [c] Eunbi Kim, [ID] [d] Taejin Jo[e] and Yong Min Lee [ID] *[a,b,c,d]

To address the difficulty in achieving both thin and wide lithium (Li) metal electrodes using conventional extrusion and pressing methods, a slurry-based coating process with lithium metal powder (LMP) is considered a promising alternative. By adjusting the coating conditions, this technique allows the fabrication of ultra-thin and wide Li metal electrodes. However, the Li_2CO_3 passivation layer formed to enhance storage stability is electrically insulating and must be mechanically disrupted prior to using the LMP electrode as an anode. The calendering process, conducted after LMP slurry coating and drying, serves as an essential step that fractures the brittle Li_2CO_3 layer and exposes the underlying fresh Li metal within the LMP particles. The exposed ductile Li directly contacts adjacent particles or the Cu current collector, thereby extending the electrically conductive network within the electrode and contributing to the formation of electrochemically active LMP. In this study, we systematically investigate how the calendering process affects the structural evolution and electrochemical activation of LMP electrodes. Under varying calendering ratios (from 0% to 40% and 40%+), we examined the correlation between electrode structural changes, Li_2CO_3 fracture, electrical connection, and the degree of electrochemical activation. Electrochemical activation increased nonlinearly with the calendering ratio, with a critical threshold near 35%. The optimal calendering conditions for LMP activation were determined through experimental validation and simulation analysis.

Broader context

Lithium (Li) metal is considered a promising anode material for next-generation batteries due to its high theoretical capacity and low redox potential. However, conventional Li metal foil manufacturing approaches face limitations in fabricating ultra-thin and wide electrodes, particularly under high-throughput processing conditions. As an alternative, a slurry-coating method using lithium metal powder (LMP) provides dimensional tunability and compatibility with continuous roll-to-roll processes for fabricating Li metal electrodes. After slurry coating onto a Cu current collector and drying, the calendering process facilitates the electrochemical activation of LMP by disrupting the insulative Li_2CO_3 passivation layer and inducing direct contact between LMP particles and the Cu current collector, thereby extending the electrically conductive network within the electrode. While previous studies have primarily focused on preserving electrochemically active LMP within the electrode, this study systematically investigates how the calendering process induces structural reconfiguration and interfacial connection to initiate and maximize the electrochemical activation of LMP. Furthermore, this study provides a detailed understanding of the electrochemical activation mechanism as a function of calendering ratio in next-generation anodes based on sodium, aluminium, or metal alloy powders.

[a]*Department of Chemical and Biomolecular Engineering, Yonsei University, Seoul 03722, Republic of Korea. E-mail: yongmin@yonsei.ac.kr*
[b]*Department of Battery Engineering, Yonsei University, Seoul 03722, Republic of Korea*
[c]*Department of Energy Science and Engineering, Daegu Gyeongbuk Institute of Science and Technology (DGIST), Daegu 42988, Republic of Korea*
[d]*Battery Conflation Engineering, Yonsei University, Seoul 03722, Republic of Korea*
[e]*Lotte Energy Materials, Seoul 06619, Republic of Korea*
† These authors contributed equally to this work.

1. Introduction

Lithium (Li) metal has regained attention as a promising anode material for next-generation rechargeable batteries due to its high theoretical capacity (3860 mAh g^{-1}), low redox potential (−3.04 V *vs.* the standard hydrogen electrode), and the development of electrolyte design and interfacial stabilization technologies.[1–3] The extrusion and pressing process is the most widely used method for fabricating Li metal foil electrodes.[4–6] However, under high-throughput production

© 2026 The Author(s). Published by the Royal Society of Chemistry

conditions, this conventional method faces challenges in fabricating ultra-thin and wide Li electrodes while achieving structural uniformity.[7–9] Vapor deposition and electroplating have been considered candidate approaches, offering advantages in fabricating thin and wide electrodes.[10–12] Nevertheless, deposition-based methods could suffer from non-uniform Li deposition under rapid production conditions, leading to dendritic growth.[13,14] As an alternative, fabricating Li metal electrodes *via* slurry casting of lithium metal powder (LMP) onto a current collector (CC) has attracted more attention.[15–18] A slurry-based coating method using LMP has been considered a promising method for Li metal electrode fabrication due to its dimensional tunability and compatibility with conventional roll-to-roll processes.[19–21] The LMP slurry, composed of LMP particles, a polymeric binder, and an organic solvent, allows the fabrication of ultra-thin (∼20 μm) and wide (∼300 mm) Li metal electrodes through a scalable coating process.[22]

Despite these processing advantages, delamination of the LMP composite layer from the CC remains a critical issue, leading to electrical contact loss and electrochemical inactivation at the interfaces of LMP particles and LMP layer/CC.[23] To ensure interfacial connectivity, a polyimide (PI) binder with strong adhesion and mechanical robustness has been introduced into LMP electrodes.[24] However, the insulating nature of the PI binder limits electron transport at the interfaces of LMP particles. Therefore, conductive additives such as multi-walled carbon nanotubes have been incorporated into the PI matrix, forming conductive carbon-binder domains that facilitate interparticle electrical connections, thereby securing the electrochemical activation of LMP electrodes.[25] In addition, adhesive-conductive interlayers have been suggested to improve the physical and electrical contact at the LMP layer/CC interface.[26] Although these approaches have contributed to preserving electrochemically activated LMP, the fundamental mechanism of electrochemical activation within the electrode remains insufficiently understood. Therefore, a detailed understanding of LMP particle-level structural and interfacial characteristics is required to clarify how LMP electrodes become electrochemically activated.

Spherical LMP particles with large surface areas readily oxidize upon exposure to air, moisture, or organic solvents. To suppress this reactivity, manufacturers such as Rio Tinto have introduced a submicron-thick Li_2CO_3 passivation layer on the particle surface.[29,30] While this layer improves storage stability and enables slurry-based electrode fabrication, its insulating nature restricts direct participation of LMP in electrical conduction for electrochemical reactions.[31] During electrode fabrication, calendering is the key process that mechanically fractures the Li_2CO_3 layer, thereby exposing metallic Li surfaces. Exposed Li forms continuous Li/Li contacts, extending to the CC to establish conductive pathways across the electrode. Simultaneously, Li/electrolyte interfaces created by surface exposure provide electrochemically active sites. In this context, calendering is thus considered to determine the development of electrical pathways and the expansion of electrochemically active interfaces in LMP electrodes.

In this study, we systematically investigate how the calendering ratio influences the electrochemical activation of LMP electrodes. Calendering simulations were conducted on electrodes with ratios from 0% to 45% to analyze von Mises stress (VMS) distributions, Li_2CO_3 fracture, and the formation of Li/Li and Li/CC contacts. Electron beam absorbed current (EBAC) measurements were employed to comparatively evaluate electrical conductivity across electrode cross-sections at different calendering ratios. Electrochemical activation was assessed in Li‖Cu cells by measuring the reversible Li stripping capacity, which reflects the electrochemically active volume of LMP particles. Li‖NCM cells in both carbonate-based electrolyte and localized high-concentration electrolyte (LHCE; LiFSI/DME/ TTE = 1/1.2/3, molar ratio) showed an optimal calendering ratio where LMP electrodes delivered performance comparable to that of Li foil.

2. Experimental

2.1. Lithium metal powder electrodes and NCM electrode

The LMP electrodes were prepared using stabilized lithium metal powder (SLMP®; D_{50} = 50 μm, Rio Tinto, UK-Australia). The LMP slurry consisted of 95 wt% LMP and 5 wt% PVdF-HFP binder (KynarFlex 2801; M_w = 477 000, Arkema, France) with NMP as the solvent (Sigma-Aldrich, USA) at a solid content of 35%.[27] The slurry was coated onto a Cu CC (11 μm, Lotte Energy Materials, Republic of Korea) using a doctor blade and dried under vacuum at 25 °C for 12 h. The dried LMP electrode with an initial thickness of 84 μm was calendered at 10–40% using a gap-control roll press machine (CLP-2025H; CIS, Republic of Korea).[28] The resulting electrodes were denoted as 10–40% cal., with the 40% cal. electrode exhibiting a thickness of approximately 50 μm. Particularly, at a target calendering ratio of 45%, the calendered LMP electrode using the controlled roll gap experienced excessive pressing load, which induced wrinkling of both the LMP layer and the CC. Consequently, the produced electrode became thicker than the 40% cal. electrode and is denoted as 40%+ cal. All electrode preparation procedures were conducted in an Ar-filled glove box (dew point <−80 °C). The $Li(Ni_{0.6}Co_{0.2}Mn_{0.2})O_2$ (NCM622, U&S Energy, Republic of Korea) cathode used for full-cell tests consisted of 96 wt% NCM622, 2 wt% conductive carbon, and 2 wt% PVdF binder, with a density of 3.5 g cm⁻³. A cathode with an areal capacity of 2.0 mAh cm⁻², corresponding to a mass loading of 11.3 mg cm⁻², was employed.

2.2. Cell assembly

Two types of 2032 coin cells—Li‖Cu and Li‖NCM622—were assembled in an Ar-filled glove box (dew point <−80 °C). Electrode diameters were 12 mm for Li and 16 mm for Cu in Li‖Cu cells, and 16 mm for Li and 12 mm for NCM622 in Li‖NCM622 cells. A PE separator (V20CFD; porosity = 43%, Tonen, Japan) with an 18 mm diameter and 20 μm thickness was employed.

The carbonate-based electrolyte consisted of 1.15 M lithium hexafluorophosphate (LiPF₆; Enchem, Republic of Korea) in

ethylene carbonate/ethyl methyl carbonate (EC/EMC = 3/7, v/v, Enchem, Republic of Korea) with 10 wt% fluoroethylene carbonate (FEC; Enchem, Republic of Korea) as an additive, and 200 μL was introduced for cathodes with an areal capacity of 2 mAh cm^{-2}. The localized high-concentration electrolyte (LHCE) consisted of lithium bis(fluorosulfonyl)imide (LiFSI; 0.57 g, 1 molar ratio, Enchem, Republic of Korea) and 1,2-dimethoxyethane (DME; 0.33 g, 1.2 molar ratio, Enchem, Republic of Korea), mixed at 200 rpm for 12 h, followed by the addition of 1,1,2,2-tetrafluoroethyl-2,2,3,3-tetrafluoropropyl ether (TTE; 2.1 g, 3 molar ratio, SynQuest Labs, USA) and further stirring at 80 rpm for 12 h. 20 μL of LHCE was introduced for the cathode with an areal capacity of 2 mAh cm^{-2}, corresponding to one-tenth of the carbonate-based electrolyte volume.

2.3. Electrochemical analysis

To quantify the electrochemically active LMP particles in the electrodes, three Li||Cu cells were assembled for each electrode condition and tested using a cycle tester (TOSCAT-3200P; Toyo, Japan). The reversible Li stripping capacity was determined by galvanostatic stripping at a current density of 0.2 mA cm^{-2} until a cut-off voltage of −1.0 V was reached. Three Li|| NCM622 cells were tested for each condition to evaluate cycling performance. After 12 h of aging at 25 °C, the formation cycle was performed at 0.1C charging/discharging. Cycling performance was tested with the carbonate-based electrolyte (charging CC/CV at 0.5C, discharging CC at 2C) and with the LHCE (charging CC/CV at 1C, discharging CC at 2C). AC impedance was measured using an impedance analyzer (VSP-300; BioLogic, France) over the frequency range of 5 MHz to 50 mHz at a root-mean-square voltage amplitude of 10 mV.

2.4. Structural characterization techniques

Field-emission scanning electron microscopy (FE-SEM, JSM-IT800(SHL); JEOL, Japan) equipped with an Ultim Extreme windowless detector (Ultim Extreme Infinityl; Oxford Instruments, UK) was employed to analyze the microstructure of LMP electrodes and to perform elemental mapping including Li. Local electrical conductivity was characterized using FE-SEM (Teneo VS; Thermo Fisher Scientific, USA) operated in EBAC mode. For EBAC analysis, cross-sectional electrode samples were mounted on the FE-SEM stage with insulating double-sided tape to ensure electrical isolation. A conductive tip was connected to the CC to provide electrical linkage between the electrode and the amplifier. A focused primary electron beam was applied, and a fraction of the incident electrons was absorbed into the electrode and transported through the conductive network. The absorbed electrons were collected at the Cu CC and transmitted through the conductive tip and external circuit using a current amplifier, where the current was measured and recorded as EBAC intensity. The electron beam was sequentially scanned across the electrode cross-section, and the absorbed current at each position was quantitatively recorded. EBAC measurements were performed at an accelerating voltage of 3 kV with a spot size of 13 nm. In EBAC

mapping, materials with higher atomic numbers (*e.g.*, Cu) generally appeared darker than lower atomic number domains (*e.g.*, Li) because their larger backscattered electron yield reduced the absorbed current.

Cross-sections of the electrodes were prepared using a cross-section polisher (IB-19510CP; JEOL, Japan) at −80 °C and 6 kV for 2 h, followed by 4 kV for 30 min. Postmortem electrodes were extracted, then rinsed with dimethyl carbonate (DMC; Enchem, Republic of Korea, H$_2$O < 10 ppm), and vacuum-dried at 25 °C for 12 h inside an Ar-filled glove box.

2.5. Simulations

With the constructed uncalendered LMP electrode reflecting the actual electrode design parameters, calendering simulations were performed to analyze microstructural evolution and mechanical stress during compression, using the ElastoDict module in GeoDict 2025, which is based on the finite volume method. Li was modeled as a perfect plastic material, while a fracture model was applied to capture the brittle mechanical behavior of Li$_2$CO$_3$. PVdF-HFP and Cu were treated as linear elastic materials. The calendering process was modeled as uniaxial compression along the thickness (*z*) direction, with symmetric boundary conditions and a strain-controlled mechanical load. Detailed governing equations and modeling parameters are provided in the SI (Tables S1–S3).

3. Results and discussion

Fig. 1 shows the LMP electrode fabrication process with three consecutive steps: (1) preparation of the LMP slurry by mixing LMP particles, polymeric binder, and organic solvent, (2) coating of the slurry onto a Cu CC followed by drying to remove the solvent, and (3) calendering of the dried electrode using a roll press machine. The slurry-based fabrication process allows precise control of coating parameters, enabling fabrication of ultra-thin and wide electrodes. Fig. S1 demonstrates a 300 mm-wide LMP electrode, validating the scalability of the coating method.

Cross-sectional SEM images and EDS mapping were conducted to examine structural changes in LMP electrodes with increasing calendering ratio (Fig. 2a–c and Fig. S2). In the 0% calendered electrode (0% cal.), the spherical morphology of LMP particles is preserved, and large pores are observed across the electrode. Isolated Li domains with limited connection to the Cu CC confirm poor interfacial contact. At 20% cal., vertical compression deformed the top and bottom surfaces of LMP particles, and this deformation induced local flattening with partial reshaping, which reduced pore volume while increasing particle/particle and particle/CC contacts. Li mapping signals become denser across the electrode, indicating improved structural continuity at the interfaces. At 40% cal., pores were further reduced, and LMP particles were compacted into polygonal shapes, forming multiple interfaces with neighboring particles and the CC. These results confirm that calendering densifies the electrode by reducing electrode
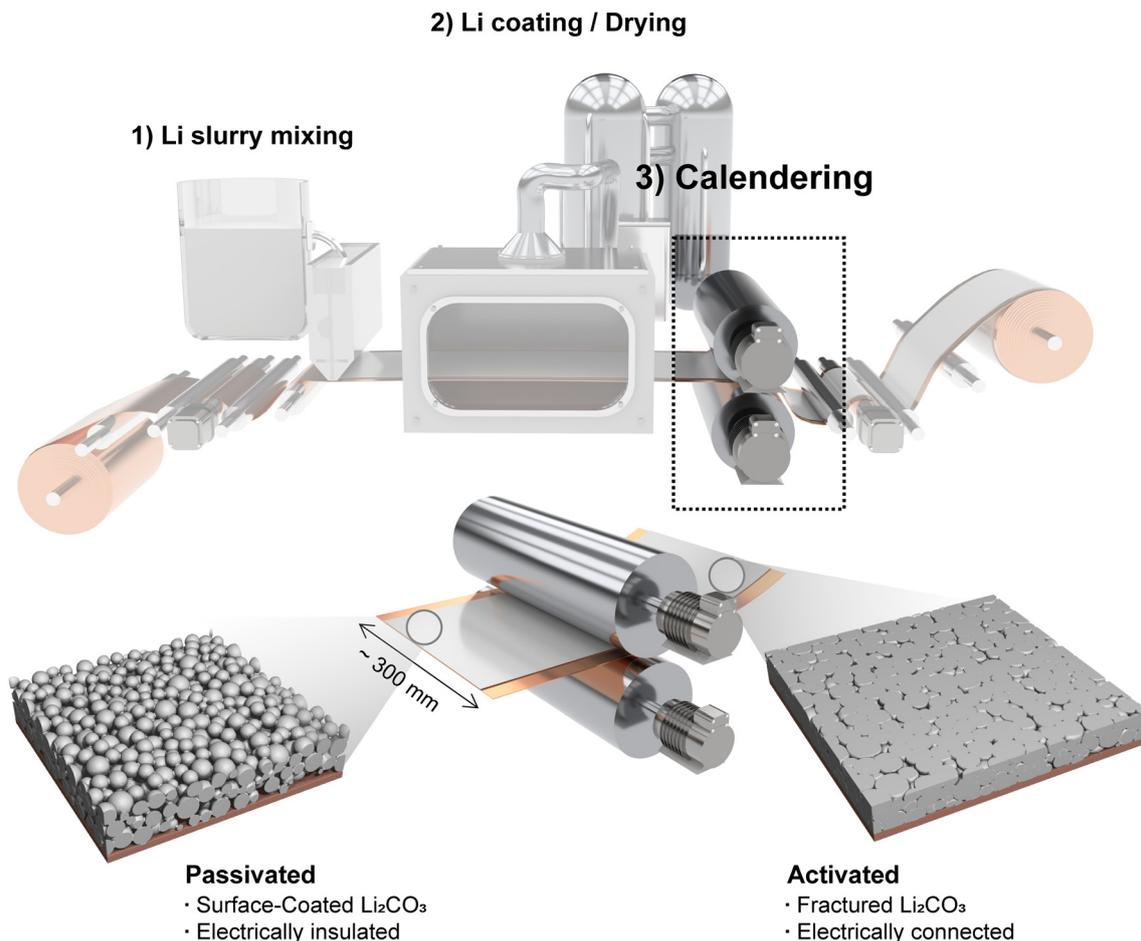
Fig. 1 Schematic illustration of slurry-based LMP electrode fabrication, including slurry mixing, coating and drying on a Cu CC, and roll-press calendering.

thickness, decreasing pore volume, and increasing interfacial contacts with both particles and the CC. During calendering, mechanical stress is concentrated on the surfaces of LMP particles and induces local fracture of the brittle Li_2CO_3 layer.

As shown in Fig. 3a, pristine LMP particles prior to the electrode fabrication process exhibit a spherical morphology without deformation. A cross-sectional SEM image acquired at the particle edge is shown in Fig. 3b. As observed in the magnified image in Fig. 3c, the surface layer exhibits a thickness variation, with the thinnest regions measuring approximately 100 nm and covering the Li metal. The corresponding oxygen EDS mapping in Fig. 3d shows that oxygen is localized within this surface layer, indicating the presence of an oxygen-rich Li_2CO_3 layer that reduces the surface reactivity of LMP particles (Fig. S3 and S4).[32] On the other hand, Fig. 3e and Fig. S5 show the morphology of LMP particles after electrode fabrication and calendering. Upon compressing particles, the applied pressure transformed the spherical geometry of LMP particles into flattened or polygonal shapes, whereas the brittle Li_2CO_3 passivation layer did not experience plastic deformation but fractured. As a result, the fractured regions expose fresh Li beneath the passivation layer.

With increasing calendering ratio, contact between exposed Li surfaces and adjacent metallic Li increased, leading to progressive expansion of Li/Li contacts across the electrode. When electrically conductive Li/Li contacts extend to the Cu CC, a continuous conductive network is formed, which enables electron supply from the CC into the electrode. Simultaneously, the increased Li/electrolyte interfacial area secures more reaction sites for Li plating and stripping. In this context, the calendering process results in the establishment of electrically conductive pathways and electrochemically active surfaces.

To systematically analyze how calendering-induced structural changes lead to electrochemical activation within LMP electrodes, mechanical compression simulations using the finite volume method were conducted under varying calendering ratios. To simulate microstructure evolution during calendering, the complex mechanical behavior of LMP (ductile) with the Li_2CO_3 passivation layer (brittle) should be considered. Accordingly, both a perfect plastic model and a failure model were employed to incorporate ductile and brittle characteristics, respectively (Fig. S6).

To generate the LMP electrode shown in Fig. 4a, the uncalendered electrode (0% cal.) structure was first constructed as
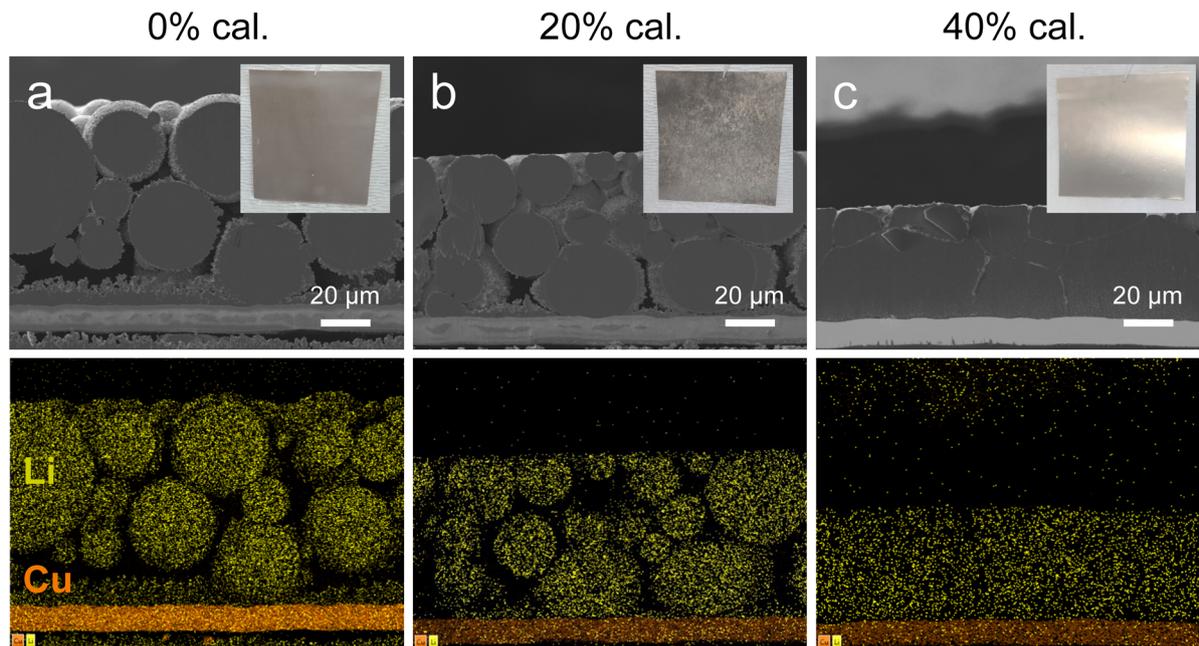
Fig. 2 Cross-sectional SEM images with the corresponding EDS mapping of LMP electrodes at different calendering ratios, including digital images of electrode surfaces at (a) 0%, (b) 20%, and (c) 40% cal.
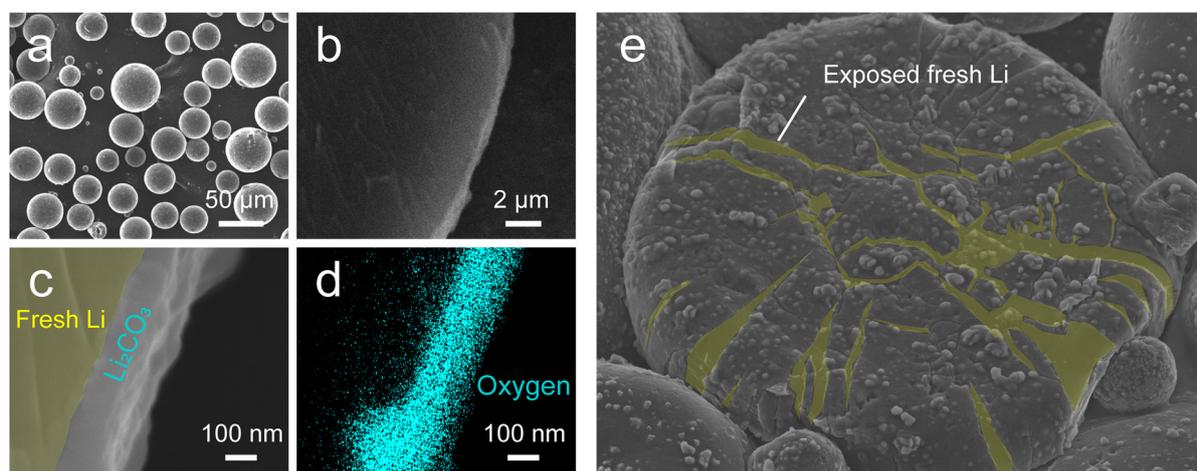

Fig. 3 SEM and EDS characterization of the Li$_2$CO$_3$ passivation layer on pristine LMP particles. (a) Top-view SEM image of LMP particles prior to electrode fabrication. (b) Cross-sectional SEM image acquired at the particle edge. (c) Magnified SEM image showing an approximately 100 nm-thick Li$_2$CO$_3$ passivation layer. (d) Corresponding oxygen EDS mapping indicating an oxygen-rich surface layer. (e) SEM image of an LMP electrode after calendering, showing fracture of the Li$_2$CO$_3$ layer and exposure of fresh Li (highlighted in yellow).

an initial state reflecting the actual electrode composition, Li$_2$CO$_3$ layer thickness (100 nm), and particle size distribution (Fig. S7). The simulation then calculated the VMS distribution as a function of the calendering ratio and identified interfacial regions where the local stress exceeds the fracture strength of the Li$_2$CO$_3$ layer (200 MPa),[33] which indicates potential Li$_2$CO$_3$ fracture and subsequent electronic/ionic connection. Thus, we assumed that once the Li$_2$CO$_3$ domains reached the fracture strength, connections between LMP and the Cu CC or electrolyte were established. Conversely, if the local stress did not

exceed the fracture strength of Li$_2$CO$_3$, the intact Li$_2$CO$_3$ layer in Fig. 4b prohibits electron or ion transport toward LMP. Notably, the VMS immediately exceeded the elastic limitation of LMP (ca. 1 MPa)[34] even under mild 10% calendering, because of the inherently deformable nature of metallic Li. However, the VMS at interfaces between LMP particle/particle and particle/Cu CC did not increase substantially at low calendering ratios, but rose sharply above 30% calendering, accompanied by distinct morphological deformation of individual particles (Fig. 4c and d). At 40% cal., stress-concentrated
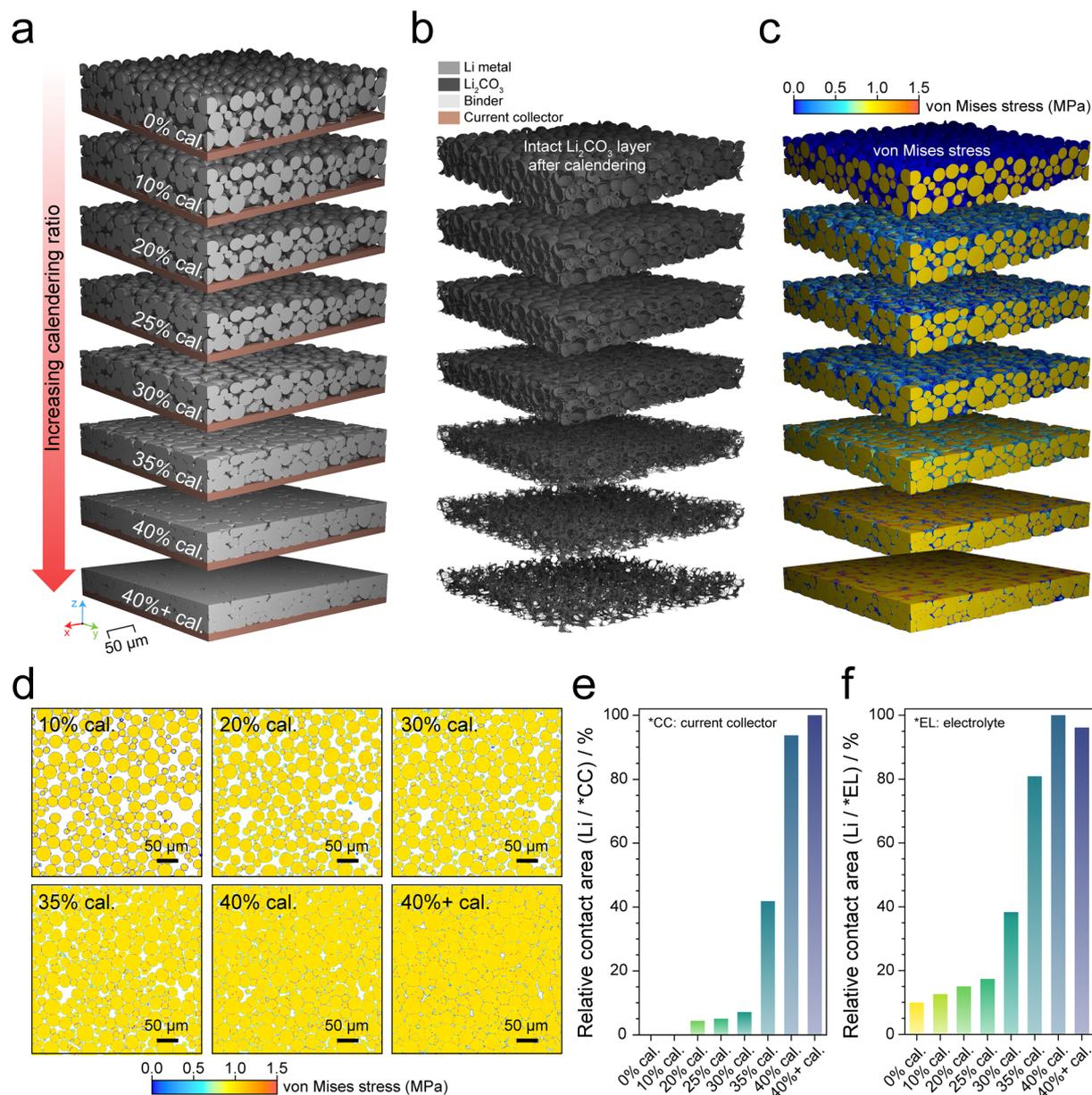
Fig. 4 Simulation-based evaluation of stress distribution and interfacial contact in LMP electrodes under varying calendering ratios. (a) 3D electrode structures obtained from calendering simulations. (b) Intact Li_2CO_3 passivation layers where the local stress did not exceed the fracture strength. (c) 3D and (d) 2D von Mises stress (VMS) distributions as a function of calendering ratio. (e) Relative contact area between LMP particles and the Cu current collector (CC), and (f) relative contact area between LMP particles and the electrolyte (EL).

regions extended throughout the electrode, and interfacial domains exceeding the fracture strength of Li_2CO_3 became widespread, significantly reducing the fraction of intact Li_2CO_3 (Fig. 4b and Fig. S8), implying the establishment of continuous conductive pathways. These results suggest that calendering creates structural conditions favorable for forming electrically conductive interfaces.

To quantitatively evaluate the interfacial contact characteristics induced by mechanical stress, simulation results were analyzed to determine both the electronic contact area (between LMP particles and Cu CC) and the ionic contact area

(between LMP and electrolyte) where local stress exceeded the fracture strength of Li_2CO_3. As shown in Fig. 4e and f, from 0% to 25% cal., the contact area between LMP particles and the Cu CC or electrolyte remained limited, even though the electrode densified and particles were rearranged, because most local stresses remained below the Li_2CO_3 fracture strength. Consequently, electronic and ionic contact remained minimal. However, at 30–35% cal., localized stress at specific interparticle interfaces surpassed the fracture strength, as confirmed by VMS analysis, leading to partial fracture and fresh Li exposure. The electrical contact area began to increase gradually, indicat-

ing the expansion of interparticle electrical connections. Additionally, owing to the planar and rigid Cu CC surface, LMP particles near the bottom of the electrode experienced direct mechanical stress, inducing more pronounced localized stress accumulation (Fig. S9). At 40% cal., the electronic and ionic contact areas rose sharply. This sharp increase indicates that electrochemical activation occurs only when concentrated stress exceeds the fracture strength of the Li_2CO_3 layer, rather than progressing gradually with calendering, which is consistent with the increased electrochemically active surface area and electrical connectivity observed in the electrochemical analysis (Fig. S10). The transition between 30% and 40% cal. validates this threshold behavior, confirming that concentrated stress surpasses the fracture strength of the Li_2CO_3 layer and thereby establishes electrochemical activation across the electrode.

Local electrical conductivity was characterized using FE-SEM operated in electron beam absorbed current (EBAC) mode (Fig. S11). This technique enables direct visualization of electron transport through the electrode cross-section, and EBAC measurements were employed to evaluate the electrical pathways in LMP electrodes with different calendering ratios (Fig. 5a).[35,36] Under focused electron beam irradiation, a fraction of the incident electrons that entered the electrode was transported through electrically conductive networks in the LMP electrode. The resulting current was collected at the Cu CC and recorded as EBAC intensity.

The EBAC line-scan profiles in Fig. 5b were measured along the electrode depth from the CC to clarify the differences in electrical conductivity within the electrode as a function of the calendering ratio. As validated in Fig. S12, the EBAC intensity is directly proportional to the measured EBAC current, confirming that the intensity reliably represents the current flow within the electrode. At 20% cal., the EBAC intensity is overall low, indicating that insulating Li_2CO_3 layers surrounded the LMP particles and caused electrical isolation, thereby limiting electron transport to the CC. At 30% cal., the EBAC intensity increases compared to that at 20% cal. and shows a higher baseline across the electrode, indicating the onset of conductive pathway formation, although electron transport continuity remains incomplete. At 40% cal., the EBAC intensity significantly increases and remains consistently high throughout the electrode thickness, indicating the formation of a continuous conductive network.

The EBAC mapping images in Fig. 5c show conductive regions across the electrode cross-sections. Because intact Li_2CO_3 layers electrically isolate the LMP particles, the EBAC intensity remains low throughout the electrode at 20% cal. By increasing the calendering ratio to 30%, the EBAC intensity becomes more pronounced inside particles and at particle/particle contact regions, suggesting the formation of local electrical connections. At 40% cal., intense EBAC signals are continuously distributed across the electrode and particle boundaries
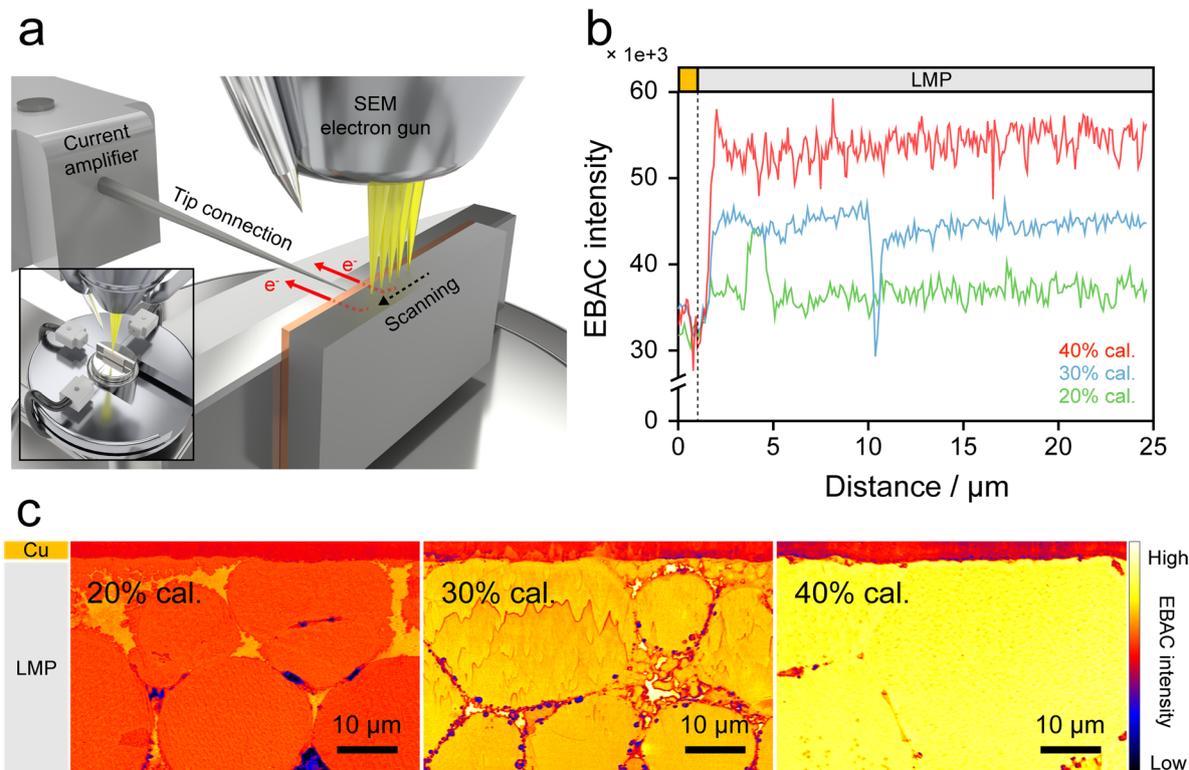

Fig. 5 Electron beam absorbed current (EBAC) analysis of LMP electrodes with different calendering ratios. (a) Schematic illustration of the EBAC measurement setup. (b) EBAC line-scan profiles along electrode depth from the Cu CC and (c) EBAC mapping images of cross-sections showing conductive pathways at 20%, 30%, and 40% cal.

merge, demonstrating the formation of a one-body conductive structure. Top-view EBAC analysis of pristine LMP particles and the 40% cal. electrode clarifies this transition (Fig. S13). EBAC mapping confirms the transition of LMP electrodes from particle-level isolation to a continuous conductive network extending across the electrode.

To quantify the electrochemically active LMP particles in the electrodes, Li‖Cu cells were assembled using electrodes with calendering ratios of 0–40% and 40+, and three cells were prepared for each condition. The reversible Li stripping capacity was determined by galvanostatic stripping at 0.2 mA cm^{-2} until −1.0 V was reached, thereby quantifying the maximum reversible Li (inset, Fig. 6a). The uncalendered electrode has an initial thickness of 84 μm, which decreased to 50 μm after 40% calendering. Intermediate electrodes were prepared by calendering the uncompressed electrode to the target ratios (Fig. S14). In the 40%+ cal. electrode, which was fabricated by compressing the electrode beyond 40% cal., the Cu CC experiences excessive load that causes localized plastic deformation of both the LMP layer and the Cu CC. Consequently, wrinkling occurs in the LMP layer and on the Cu CC surface, and the apparent thickness exceeds 50 μm (Fig. S15).

As shown in Fig. 6a, the stripping capacity increases with the calendering ratio. Notably, the reversible Li source increases markedly beyond 30% cal., consistent with the calendering simulation in which fracture of the Li$_2$CO$_3$ passivation layer on LMP particle surfaces was pronounced at ≥35% cal. As shown in Tables S4 and S5, the degree of electrochemical activation was defined as the ratio of the experimental Li stripping capacity to the theoretical capacity of the LMP electrode. Fig. 6b indicates that the 0% and 10% cal. electrodes exhibit negligible activation, implying the absence of effective electrical pathways. At 20% cal., the degree of activation reaches 6%, indicating limited particle deformation and insufficient interparticle contact. With further increases to 25%, 30%, and 35% cal., the activation increases to 11%, 22%, and 56%, respectively, in accordance with the progressive collapse of voids and expansion of electrical contacts. In contrast, the 40% cal. exhibits a substantial increase to 93%, which validates that a continuous electrical network is fully established across the electrode. The 40%+ cal. electrode also exhibits a degree of electro-
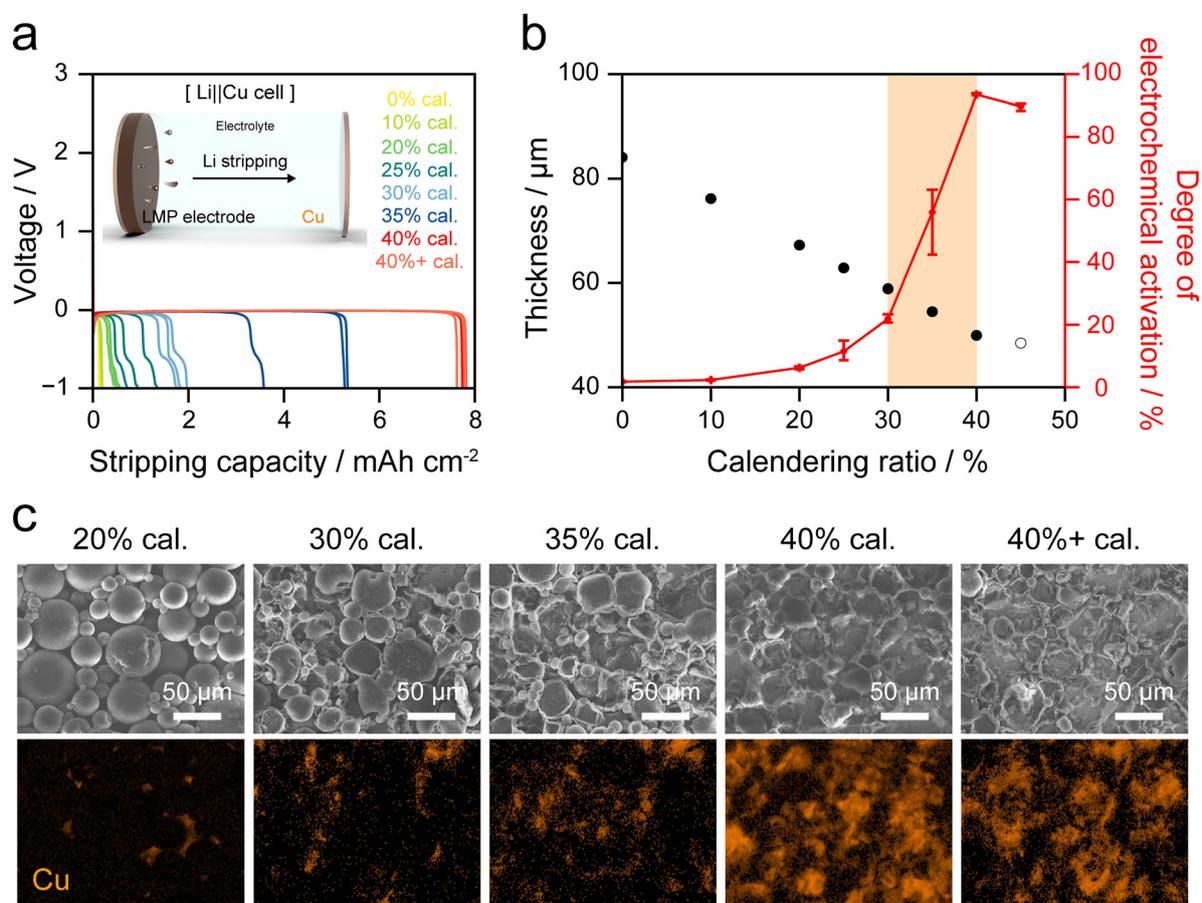

Fig. 6 Electrochemical activation of LMP electrodes with different calendering ratios. (a) Voltage profiles of Li stripping at 0.2 mA cm^{-2} (cut-off: −1 V), showing data from three individual cells for each condition. The inset illustrates Li stripping from the LMP electrode in a Li‖Cu cell. (b) Degree of electrochemical activation as a function of calendering ratio, defined as the ratio of stripped Li relative to theoretical capacity. (c) Postmortem SEM and Cu EDS mapping images of electrode surfaces at 20–40% and 40%+ cal. after Li stripping until cut-off voltage.

chemical activation above 90%, comparable to that of the 40% cal. electrode.

After Li stripping to −1 V in Li||Cu cells, SEM and Cu EDS mapping were conducted to examine the surface morphology of LMP electrodes (Fig. 6c). At 20% cal., most LMP particles remain electrochemically inactive, resulting in Cu signals being barely detected. At 35% cal., over 50% of the LMP particles are activated, and Cu signals appear across wider regions of the CC. In contrast, at 40% cal. and 40%+ cal., more than 90% of the Li source is stripped from the LMP electrode. As a result, only a minor residual composed of the binder and a small fraction of inactive LMP particles remains on the Cu CC surface, and Cu mapping reveals dense signals across the surface.

To investigate the influence of calendering ratio on the electrochemical behavior of LMP electrodes, Li||NCM622 full cells (2.0 mAh cm^{-2}) were assembled using the carbonate-based electrolyte. Fig. 7a clearly confirms the correlation between electrochemical activation of LMP particles and Li plating behavior on the electrode. After the first charging at 0.1C in the precycle, electrode cross-sections were analyzed by SEM. Since electrochemically activated LMP particles are negligible in 0% cal., electrochemical reactions occur only on the Cu CC surface. Therefore, Li$^+$ released from the NCM cathode deposits preferentially on the Cu CC rather than on the inactive LMP surface. At 30% cal., reduced porosity suppresses Li plating on

the Cu CC, while partial activation enables Li plating on the upper regions of the LMP layer (Fig. S16). Fig. S17–S20 present simulation results indicating that Li$^+$ percolation pathways depend on the pore structure during calendering. From 35% cal., activation of a significant fraction of LMP particles facilitates Li plating across broader regions of the electrode, which results in a more uniform deposition. At 40% cal. and above, most LMP particles are electrochemically activated, and continuous Li plating occurs throughout the electrode thickness, which confirms that calendering establishes a one-body conductive and electrochemically active structure.

Fig. 7b presents the long-term cycling performance of LMP electrodes in Li||NCM622 full cells. Three cells for each condition were cycled at 0.5C charging and 2C discharging using the carbonate-based electrolyte. Fig. S21 shows the corresponding voltage profiles at the 1st, 50th, 100th, 200th, 400th, and 500th cycles. Electrodes with 0–30% cal. exhibit rapid capacity fading, with retention dropping below 80% within 30 cycles, due to limited electrochemical activation and side reactions associated with dendritic and porous Li structures. At 35% cal., partial utilization of LMP particles in electrochemical reactions enables capacity retention of 80% up to 70 cycles. With further calendering, the 40% cal. electrode achieves stable cycling for more than 300 cycles at 80% retention, comparable to a 50 μm-thick Li foil sample (equivalent to *ca.*
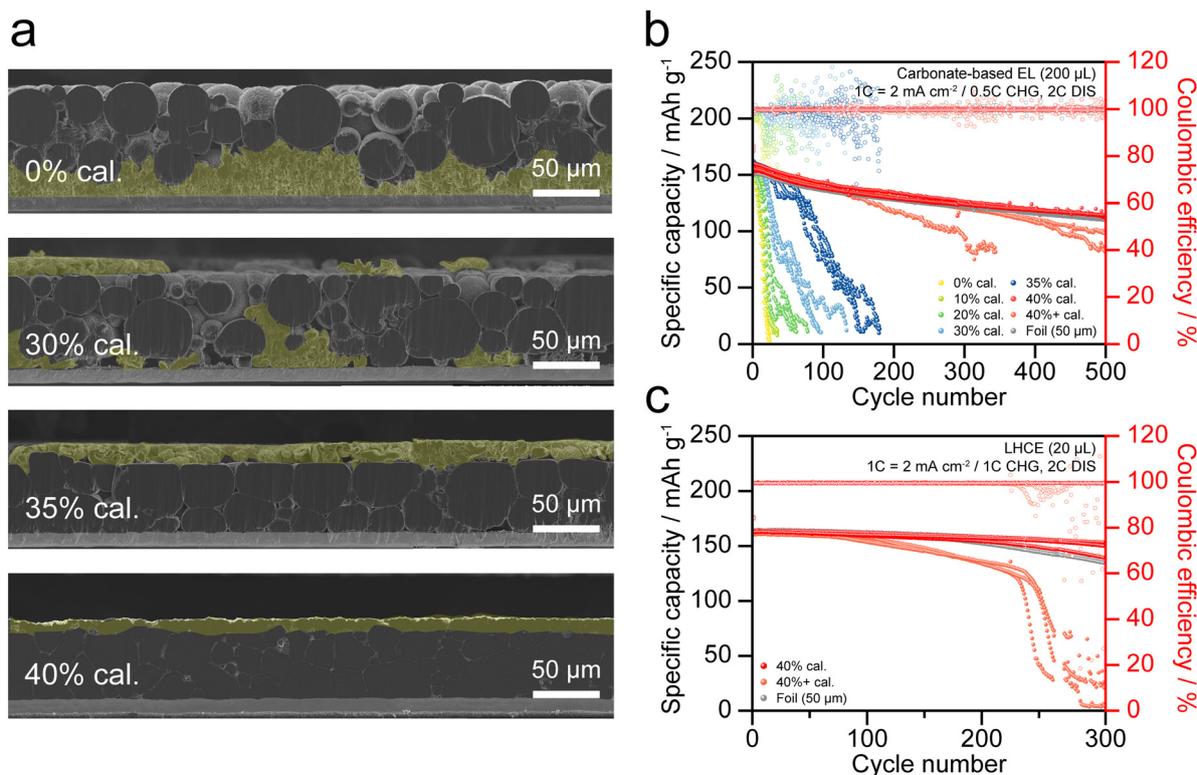

Fig. 7 Electrochemical performance of LMP electrodes with different calendering ratios in Li||NCM622 (2 mAh cm^{-2}) full cells. (a) Cross-sectional SEM images after initial 0.1C charging, highlighted in yellow regions indicating Li deposition at 0–40% cal. Cycling performance (b) of 0–40%+ cal. electrodes and Li foil at 0.5C charging and 2C discharging in the carbonate-based electrolyte (1.15 M LiPF$_6$ in EC/EMC = 3/7, v/v, with 10 wt% FEC) and (c) of 40% cal., 40%+ cal. electrodes and Li foil under 1C charging and 2C discharging in the LHCE (LiFSI/DME/TTE = 1/1.2/3, molar ratio).

10 mAh cm^{-2}). In contrast, the 40%+ cal. electrode shows large cell-to-cell variations. Only one cell demonstrates stability similar to the 40% cal. electrode, whereas the other two degrade to 80% retention within 200 cycles. The observed cell-to-cell variation for the 40%+ cal. electrode suggests the presence of an optimal calendering ratio for maximizing electrochemical performance.

Validation under reduced electrolyte content is required to realize high-energy-density Li metal batteries. Compared with the analysis conditions in Fig. 7b, the electrolyte volume was reduced from 200 to 20 μL. Because carbonate-based electrolytes are highly reactive with Li metal, the ether-based LHCE containing DME and TTE was employed. Fig. 7c presents the discharge capacities of 40% cal., 40%+ cal., and Li foil, with the corresponding voltage profiles at the 1st, 50th, 100th, and 200th cycle provided in Fig. S22. As previously observed, the 40%+ cal. electrode shows larger cell-to-cell variations, with the median retention of three cells reaching 80% at the 230th cycle. In contrast, the 40% cal. electrode shows 95% capacity retention at the 250th cycle, showing performance comparable to that of Li foil. These results confirm that the fully activated LMP electrode delivers electrochemical performance comparable to that of Li foil, while maintaining dimensional tunability and compatibility with continuous roll-to-roll fabrication.

4. Conclusion

In this study, the structural and electrochemical responses of slurry-based LMP electrodes to calendering ratios from 0% to 40% and 40%+ were investigated. Progressive compression fractured the Li$_2$CO$_3$ surface layer, exposed metallic Li, and promoted interparticle and particle/Cu CC interface contacts, which transformed the electrode from a porous network into a conductive one-body structure. This structural transition was validated by EBAC mapping and line-scan analysis. Electrochemical analyses revealed a nonlinear activation trend, and a distinct threshold was identified at approximately 35% calendering. At 40% cal., interfacial contact became continuous, >90% of the theoretical Li capacity was accessed, and Li‖NCM622 full cells delivered cycling stability comparable to 50 μm Li foil. In contrast, a calendering ratio of 40%+ induced Cu CC deformation and performance variability, confirming the mechanical limitation of excessive compression. These results demonstrate that approximately 40% calendering is the critical condition for full activation and stable electron transport pathways. Furthermore, the slurry-based fabrication strategy provides dimensional flexibility and process compatibility and, under the optimal calendering conditions, achieves electrochemical performance equivalent to that of Li foil.

Author contributions

D. K., S. H. K., and J. L. contributed equally to this work. D. K. and S. H. K. conceived the research concept, designed the experiments, and analyzed the data. S. H. K. performed the electrochemical measurements. J. L. conducted the calendering simulations. H. K., C. B. D., and E. K. assisted in materials characterization. T. J. supplied the materials. Y. M. L. supervised the overall research. All authors discussed the results and revised the manuscript.

Conflicts of interest

There are no conflicts to declare.

Data availability

All data supporting this article are available in the Supplementary Information, which contains supplementary data; twenty-two figures; and five tables. See DOI: https://doi.org/10.1039/d5eb00195a.

Acknowledgements

References

1 S. Ko, T. Obukata, T. Shimada, N. Takenaka, M. Nakayama, A. Yamada and Y. Yamada, *Nat. Energy*, 2022, **7**, 1217–1224.

2 Y. Zhang, T. T. Zuo, J. Popovic, K. Lim, Y. X. Yin, J. Maier and Y. G. Guo, *Mater. Today*, 2020, **33**, 56–74.

3 A. K. Mishra, J. Parmar and I. Mukhopadhyay, *J. Energy Storage*, 2024, **87**, 111421.

4 B. Acebedo, M. C. Morant-Miñana, E. Gonzalo, I. Ruiz de Larramendi, A. Villaverde, J. Rikarte and L. Fallarino, *Adv. Energy Mater.*, 2023, **13**, 2203744.

5 R. Schmuch, R. Wagner, G. Hörpel, T. Placke and M. Winter, *Nat. Energy*, 2018, **3**, 267–278.

6 M. Burton, S. Narayanan, B. Jagger, L. F. Olbrich, S. Dhir, M. Shibata, M. J. Lain, R. Astbury, N. Butcher, M. Copley, T. Kotaka, Y. Aihara and M. Pasta, *Nat. Energy*, 2025, **10**, 135–147.

7 J. Liu, Z. Bao, Y. Cui, E. J. Dufek, J. B. Goodenough, P. Khalifah, Q. Li, B. Y. Liaw, P. Liu, A. Manthiram, Y. S. Meng, V. R. Subramanian, M. F. Toney, V. V. Viswanathan, M. S. Whittingham, J. Xiao, W. Xu, J. Yang, X.-Q. Yang and J.-G. Zhang, *Nat. Energy*, 2019, **4**, 180–186.

8 J. Du, W. Wang, M. Wan, X. Wang, G. Li, Y. Tan, C. Li, S. Tu and Y. Sun, *Adv. Energy Mater.*, 2021, **11**, 2102259.

9 S. Kim, G. Park, S. J. Lee, S. Seo, K. Ryu, C. H. Kim and J. W. Choi, *Adv. Mater.*, 2023, **35**, 2206625.

10 Y. Zhao, S. Li, X. Huang, W. Chen, C. Wang, X. Tang, H. Dou and X. Zhang, *Small*, 2024, **20**, 2312129.

11 C. Lee, B. T. Na, J.-Y. Hur, H. Lee, H. Honma, O. Takai and J.-H. Noh, *J. Electrochem. Sci. Technol.*, 2025, **16**, 388–398.

12 N. Rospars, M. Srout, C. Fu, G. Mourouga, M. Mensi and A. Ingenito, *Commun. Mater.*, 2024, **5**, 179.

13 X. Sun, X. Zhang, Q. Ma, X. Guan, W. Wang and J. Luo, *Angew. Chem., Int. Ed.*, 2020, **59**, 6665–6674.

14 G. Lu, J. Nai, D. Luan, X. Tao, W. Xiong and D. Lou, *Sci. Adv.*, 2023, **9**, eadf1550.

15 K. Ssendagire, B. H. Lee, D. W. Ham, M. H. Jeong, J. Kim, I. Phiri and S. Y. Ryou, *J. Power Sources*, 2025, **658**, 238183.

16 J. Heine, U. Rodehorst, X. Qi, J. P. Badillo, C. Hartnig, U. Wietelmann, M. Winter and P. Bieker, *Electrochim. Acta*, 2014, **138**, 288–293.

17 A. Kolesnikov, D. Zhou, M. Kolek, J. P. B. Jimenez, P. Bieker, M. Winter and M. C. Stan, *J. Electrochem. Soc.*, 2019, **166**, A1400.

18 A. Kolesnikov, M. Kolek, J. F. Dohmann, F. Horsthemke, M. Börner, P. Bieker, M. Winter and M. C. Stan, *Adv. Energy Mater.*, 2020, **10**, 2000017.

19 D. Jin, Y. Roh, T. Jo, M.-H. Ryou, H. Lee and Y. M. Lee, *Adv. Energy Mater.*, 2021, **11**, 2003769.

20 D. Kang, M. Jeong, S. Kim, M. Song, C. B. Dzakpasu, S. H. Kim, J. Lim, S. Eom, S. Jung, J. Jang, S. Jo, H. Jeon, H. Lee, S. Choi, T. Jo, H. Lee, D. Y. Ryu, J. Kim and Y. M. Lee, *Adv. Energy Mater.*, 2025, **15**, e05780.

21 S. W. Hwang, J. H. Yom, S. M. Cho and W. Y. Yoon, *ACS Appl. Mater. Interfaces*, 2017, **9**, 22530–22538.

22 D. Kang, D. Jin, J. Moon, C. B. Dzakpasu, H. Lee, S. Choi, T. Jo, H. Lee, S. Y. Ryou and Y. M. Lee, *Chem. Eng. J.*, 2023, **452**, 139409.

23 C. B. Dzakpasu, D. Kang, D. Kim, M. Song, D. Jin, S. Y. Ryou and Y. M. Lee, *Small Struct.*, 2024, **5**, 2300476.

24 D. Jin, H. S. Bae, J. Hong, S. Kim, J. Oh, K. Kim, T. Jo, Y. M. Lee, Y. G. Lee and M. H. Ryou, *Electrochim. Acta*, 2020, **364**, 136878.

25 C. B. Dzakpasu, D. Jin, D. Kang, N. Kim, T. Jo, H. Lee, S. Y. Ryou and Y. M. Lee, *Electrochim. Acta*, 2022, **430**, 141093.

26 D. Jin, Y. Roh, T. Jo, D. O. Shin, J. Song, J. Y. Kim, Y. G. Lee, H. Lee, M. H. Ryou and Y. M. Lee, *Chem. Eng. J.*, 2021, **406**, 126834.

27 A. Kolesnikov, T. Wulfers, M. Kolek, P. Bieker, M. C. Stan and M. Winter, *Energy Technol.*, 2022, **10**, 2100871.

28 J. Heine, S. Krüger, C. Hartnig, U. Wietelmann, M. Winter and P. Bieker, *Adv. Energy Mater.*, 2014, **4**, 1300815.

29 B. M. Song, H. E. Park, W. Y. Yoon and B. K. Kim, *J. Korean Phys. Soc.*, 2009, **54**, 1136–1140.

30 S. T. Hong, J. S. Kim, S. J. Lim and W. Y. Yoon, *Electrochim. Acta*, 2004, **50**, 535–539.

31 K. Ssendagire, I. Phiri and S.-Y. Ryou, *ACS Appl. Mater. Interfaces*, 2025, **17**, 29757–29769.

32 N. Hornsveld, B. Put, W. M. M. Kessels, P. M. Vereecken and M. Creatore, *RSC Adv.*, 2017, 7, 41359–41368.

33 H. Ye, S. Gui, Z. Wang, J. Chen, Q. Liu, X. Zhang, P. Jia, Y. Tang, T. Yang, C. Du, L. Geng, H. Li, Q. Dai, Y. Tang, L. Zhang, H. Yang and J. Huang, *ACS Appl. Mater. Interfaces*, 2021, **13**, 44479–44487.

34 S. S. Behara, J. Thomas and A. Van der Ven, *Chem. Mater.*, 2024, **36**, 7370–7387.

35 Y. Huang, M. Shaibani, Md. J. Abedin, D. J. Mendoza, Z. Xu, T. D. Gamot, M. C. D. Cooray, M. Lin, G. Garnier, M. R. Hill and M. Majumder, *Adv. Energy Mater.*, 2022, **12**, 2202474.

36 Y.-K. Hong, J.-H. Kim, N.-Y. Kim, K.-S. Oh, H.-I. Kim, S. Ryu, Y. Ko, J.-Y. Kim, K.-H. Lee and S.-Y. Lee, *Nano-Micro Lett.*, 2025, **17**, 112.